

Unveiling the thermal and magnetic map of neutron star surfaces through their X-ray emission: method and lightcurves analysis

Silvia Zane¹ and Roberto Turolla²

¹*Mullard Space Science Laboratory, University College London, Holmbury St. Mary, Dorking Surrey, RH5 6NT, UK; sz@mssl.ucl.ac.uk*

²*Department of Physics, University of Padua, via Marzolo 8, I-35131, Padova, Italy; turolla@pd.infn.it*

Accepted...Received...

ABSTRACT

Recent *Chandra* and *XMM-Newton* observations of a number of X-ray “dim” pulsating neutron stars revealed quite unexpected features in the emission from these sources. Their soft thermal spectrum, believed to originate directly from the star surface, shows evidence for a phase-varying absorption line at some hundred eVs. The pulse modulation is relatively large (pulsed fractions in the range $\sim 12\%$ – 35%), the pulse shape is often non-sinusoidal, and the hard X-ray color appears to be anti-correlated in phase with the total emission. Moreover, the prototype of this class, RX J0720.4-3125, has been found to undergo rather sensible changes both in its spectral and timing properties over a timescale of a few years. All these new findings seem difficult to reconcile with the standard picture of a cooling neutron star endowed with a purely dipolar magnetic field, at least if surface emission is produced in an atmosphere on top of the crust. In this paper we explore how a dipolar+quadrupolar star-centered field influence the properties of the observed lightcurves. The phase-resolved spectrum has been evaluated accounting for both radiative transfer in a magnetized atmosphere and general relativistic ray-bending. We computed over 78000 lightcurves varying the quadrupolar components and the viewing geometry. A comparison of the data with our model indicate that higher order multipoles are required to reproduce the observations.

Key words: Radiative transfer — stars: neutron — pulsars: general — X-rays: stars — stars: individual (RX J0720.4-3125, RX J0420.0-5022, RX J0806.4-4123, RBS 1223, RBS 1774)

1 INTRODUCTION

Over the last few years a number of high resolution spectral and timing observations of thermally emitting neutron stars (NSs) have become available thanks to new generation X-ray satellites (both *Chandra* and *XMM-Newton*), opening new perspectives in the study of these sources. Thermal emission from isolated NSs is presently observed in more than 20 sources, including active radio pulsars, soft γ -repeaters, anomalous X-ray pulsars, Geminga and Geminga-like objects, and X-ray dim radio-silent NSs. There is by now a wide consensus that the soft, thermal component directly originates from the surface layers as the star cools down. If properly exploited, the information it conveys are bound to reveal much about the physics of neutron stars, shedding light on their thermal and magnetic surface distribution and ultimately probing the equation of state of matter at supra-nuclear densities.

Although thermal surface emission seems indeed to be an ubiquitous feature in isolated NSs, a power-law, non-thermal component (likely produced in the star magnetosphere) is present in most sources, where it often dominates the X-ray spectrum. Moreover, the intrinsic X-ray emission from young radio-pulsars may be significantly contaminated by the contribution of the surrounding supernova remnant. In this respect the seven dim X-ray sources discovered by *ROSAT* (hereafter XDINSs) are a most notable exception. In a sense, one may claim that these are the only “genuinely isolated” NSs and their soft thermal emission is unmarred by (non-thermal) magnetospheric activity nor by the presence of a supernova remnant or a binary companion (see e.g. Treves et al. 2000 and Haberl 2004 for reviews; Zane et al. 2005). XDINSs play a key role in compact objects astrophysics: these are the only sources in which we can have a clean view of the compact star surface, and as such offer an

unprecedented opportunity to confront theoretical models of neutron star surface emission with observations.

The XDINSs X-ray spectrum is with no exception blackbody-like with temperatures in the range $\sim 40\text{--}100$ eV and, thus far, pulsations have been detected in five sources, with periods in the range 3–11 s (see Table 1 and refs. therein). In each of the five cases the pulsed fraction is relatively large ($\sim 12\text{--}35\%$). Quite surprisingly, and contrary to what one would expect in a simple dipolar geometry, often the hardness ratio is minimum at the pulse maximum (Cropper et al. 2001; Haberl et al. 2003). Broad absorption features have been detected around $\sim 300\text{--}700$ eV in all pulsating XDINSs and the line strength appears to vary with the pulse phase. In addition, the X-ray light curves exhibit a certain asymmetry, with marked deviations from a pure sinusoidal shape at least in the case of RBS 1223 (Haberl et al. 2003; Schwöpe et al. 2005). XDINSs were unanimously believed to be steady sources, as indicated by several years of observations for the brightest of them. Unexpectedly, and for the first ever time, *XMM-Newton* observations have recently revealed a substantial change in the spectral shape and pulse profile of the second most luminous source, RX J0720.4-3125, over a timescale of ~ 2 yr (De Vries et al. 2004; Vink et al. 2004). Possible variations in the pulse profile of RX J0420.0-5022 over a similar timescale (~ 0.5 yr) have also been reported, although only at a low significance level (Haberl et al. 2004).

In the standard picture, emission from an isolated, cooling NS arises when thermal radiation originating in the outermost surface layers traverses the atmosphere which covers the star crust. Although the emerging spectrum is thermal, it is not a blackbody because of radiative transfer in the magnetized atmosphere and the inhomogeneous surface temperature distribution. The latter is controlled by the crustal magnetic field, since thermal conductivity across the field is highly suppressed, and bears the imprint of the field topology. Besides the spectrum, radiative transfer and the surface temperature distribution act together in shaping the X-ray lightcurve. Pulse profiles produced by the thermal surface distribution induced by a simple core-centered dipolar magnetic field have been investigated long ago by Page (1995), under the assumption that each surface patch emits (isotropic) blackbody radiation. Because of gravitational effects and of the smooth temperature distribution (the temperature monotonically decreases from the poles to the equator), the pulse modulation is quite modest (pulsed fraction $\lesssim 10\%$) for reasonable values of the star radius. Moreover, being the temperature distribution symmetric about the magnetic equator, the pulse shape itself is always symmetrical, regardless of the viewing geometry. Larger pulsed fractions may be reached by the proper inclusion of an atmosphere. In fact, in a strongly magnetized medium photon propagation is anisotropic and occurs preferentially along the field (magnetic beaming, e.g. Pavlov et al. 1994). Nevertheless, retaining a dipolar temperature distribution will always result in a symmetric pulse profile.

The quite large pulsed fraction, pulse asymmetry, and possibly long-term variations, recently observed in XDINSs seem therefore difficult to explain by assuming that the thermal emission originates at the NS surface, at least when assuming that the thermal surface distribution is that induced by a simple core-centered dipolar magnetic field. It

should be stressed that, although the dipole field is a convenient approximation, the real structure of NSs magnetic field is far from been understood, e.g. it is still unclear if the field threads the entire star or is confined in the crust only (e.g. Geppert, Küker & Page 2004 and references therein). Whatever the case, there are both observational and theoretical indications that the NS surface field is “patchy” (e.g. Geppert, Rheinhardt & Gil 2003; Urpin & Gil 2004 and references therein). The effects of a more complex field geometry have been investigated by Page & Sarmiento (1996), who considered a star-centered dipole+quadrupole field, again assuming isotropic emission. The presence of multipolar components induces large temperature variations even between nearby regions and this results in larger pulsed fractions and asymmetric pulse profiles.

The high quality data now available for thermally emitting NSs, and XDINSs in particular, demand for a detailed modelling of surface emission to be exploited to a full extent. Such a treatment should combine both an accurate formulation of radiation transport in the magnetized atmosphere and a quite general description of the thermal and magnetic surface distributions, which, necessary, must go beyond the simple dipole approximation. The ultimate goal is to produce a completely self-consistent model, capable to reproduce simultaneously both the spectral and timing properties. In this paper we take a first step in this direction and present a systematic study of X-ray lightcurves from cooling NSs, accounting for both a quadrupolar magnetic field (in addition to the core-centered dipole) and radiative transfer in the magnetized atmosphere. We computed over 78000 model lightcurves, exploring the entire parameter space, both in the geometrical angles and the quadrupolar components. This large dataset has been analyzed using multivariate statistical methods (the principal component analysis and the cluster analysis) and we show that a non-vanishing quadrupolar field is required to reproduce the observed XDINS pulse profiles.

2 THE MODEL

2.1 Going Quadrupolar

In this section we describe the approach we use to compute the phase-dependent spectrum emitted by a cooling NS as seen by a distant observer. This issue has been addressed by several authors in the past under different assumptions, and basically divides into two steps. The first involves the computation of the local (i.e. evaluated by an observer at the star surface) spectrum emitted by each patch of the star surface while the second requires to collect the contributions of surface elements which are “in view” at different rotation phases, making proper account for the fact that only rays propagating parallel to the line-of-sight (LOS) actually reach the distant observer. Details on each are presented in the following two subsections (§§ 2.2, 2.3) and further in Appendix A; here we discuss some general assumptions which are at the basis of our model.

We take the neutron star to be spherical (mass M , radius R) and rotating with constant angular velocity $\omega = 2\pi/P$, where P is the period. Since XDINSs are slow rotators ($P \approx 10$ s), we can describe the space-time outside

the NS in terms of the Schwarzschild geometry (see e.g. Cadeau, Leahy & Morsink 2005 for a more complete discussion about the effects of rotation).

The star magnetic field is assumed to possess a core-centered dipole+quadrupole topology, $\mathbf{B} = \mathbf{B}_{dip} + \mathbf{B}_{quad}$. Introducing a polar coordinate system whose axis coincides with the dipole axis, the (polar) components of the dipole field at the star surface are

$$B_{dip,r} = f_{dip} B_p \cos \theta \quad (1)$$

$$B_{dip,\theta} = g_{dip} B_p \sin \theta / 2 \quad (2)$$

$$B_{dip,\phi} = 0, \quad (3)$$

where B_p is the field strength at the magnetic pole, θ and ϕ are the magnetic colatitude and azimuth. The functions f_{dip} and g_{dip} account for the effect of gravity and depend on the dimensionless star radius $x \equiv R/R_S$ with $R_S = 2GM/c^2$; their explicit expressions can be found in Page & Sarmiento (1996, see also references therein). The quadrupolar field can be easily derived from the spherical harmonics expansion and its expression, again at $r = R$, can be cast in the form

$$\mathbf{B}_{quad} = \sum_{i=0}^4 q_i \mathbf{B}_{quad}^{(i)} \quad (4)$$

where the q_i 's are arbitrary constants. The polar components of the five generating vectors $\mathbf{B}_{quad}^{(i)}$ are reported in Page & Sarmiento (1996). We just note that their expression for the radial component of the zeroth vector contains a misprint and should read $B_{quad,r}^{(0)} = (3 \cos^2 \theta - 1)/2$. General relativistic effects are included in the quadrupolar field by multiplying the radial and angular components by the two functions $f_{quad}(x)$ and $g_{quad}(x)$ respectively (see again Page & Sarmiento 1996 for their expressions and further details).

The NS surface temperature distribution, T_s , will in general depend on how heat is transported through the star envelope. Under the assumption that the field does not change much over the envelope scale-height, heat transport can be treated (locally) as one-dimensional. The surface temperature then depends only on the angle between the field and the radial direction, $\cos \alpha = \mathbf{B} \cdot \mathbf{n}$, and on the local field strength B (see Page 1995). As shown by Greenstein & Hartke (1983), a useful approximation is to write

$$T_s = T_p \left(\cos^2 \alpha + \frac{K_{\perp}}{K_{\parallel}} \sin^2 \alpha \right)^{1/4} \quad (5)$$

where the ratio of the conductivities perpendicular (K_{\perp}) and parallel (K_{\parallel}) to the field is assumed to be constant. The polar value T_p fixes the absolute scale of the temperature and is a model parameter (Page 1995 and references therein). For field strengths $\gg 10^{11}$ G, the conductivity ratio is much less than unity and eq. (5) simplifies to

$$T_s = T_p |\cos \alpha|^{1/2}. \quad (6)$$

This expression is used in the present investigation. An example of the thermal surface distribution induced by a quadrupolar field is shown in figure 1. Different approaches which account for the variation of the conductivities (e.g. Heyl & Hernquist 1998) yield similar results. Quite recently

Geppert, Küker & Page (2004) investigated the influence of different magnetic field configurations on the surface temperature distribution. They find that, contrary to star-centered core fields, crustal fields may produce steeper surface temperature gradients. The inclusion of this effect is beyond the purpose of this first paper. However, we caveat that, for temperatures expected in XDINs ($\approx 10^6$ K), the differences between the two magnetic configurations start to be significant when the field strength is $> 10^{13}$ G.

2.2 Radiative Transfer

The properties of the radiation spectrum emitted by highly magnetized, cooling NSs have been thoroughly discussed in the literature (e.g. Shibano et al. 1992; Pavlov et al. 1994; Zane et al. 2001; Ho & Lai 2001; Ho & Lai 2003). Since the pressure scale-height is much smaller than the star radius, model atmospheres are usually computed in the plane parallel approximation. Besides surface gravity, the spectrum emerging from each plane parallel slab depends both on the surface temperature T_s and magnetic field \mathbf{B} , either its strength and orientation with respect to the local normal, which coincides with the unit vector in the radial direction \mathbf{n} . In order to proceed we introduce a (θ, ϕ) mesh which naturally divides the star surface into a given number of patches. Once the magnetic field has been specified, each surface element is characterized by a precise value of B , α and T_s . The atmospheric structure and radiative transfer can be then computed locally by approximating each atmospheric patch with a plane parallel slab, infinitely extended in the transverse direction and emitting a total flux σT_s^4 .

Radiative transfer is solved numerically using the approach described in Lloyd (2004). The code is based on the normal mode approximation for the radiation field propagating in a strongly magnetized medium and incorporates all relevant radiative processes. The full angle and energy dependence in both the plasma opacities and the radiation intensity is retained. In this respect we note that for an oblique field [i.e. $(\mathbf{B}/B) \cdot \mathbf{n} \neq 1$] the intensity is not symmetric around \mathbf{n} and depends explicitly on both propagation angles. If \mathbf{k} is a unit vector along the photon direction, at depth τ in the atmosphere the intensity has the form $I = I_E(\tau, \mu, \varphi)$ where E is the photon energy, $\mu = \mathbf{n} \cdot \mathbf{k}$ and φ is the associated azimuth. Calculations are restricted to a completely ionized H atmosphere (see Ho et al. 2003 and Potekhin & Chabrier 2003 for a treatment of ionization in H atmospheres).

Since the numerical evaluation of model atmospheres is computationally quite demanding, especially for relatively high, oblique fields and $T_s < 10^6$ K, we preferred to create an archive beforehand, by computing models for pre-assigned values of $\cos \alpha$, B and T_s . The range of the latter two parameters should be wide enough to cover the surface variation of B and T in all the cases of interest: $12 \leq \log B \leq 13.5$ and $5.4 \leq \log T_s \leq 6.6$. Particular care was taken to generate models in the entire α domain, $0 \leq \cos \alpha \leq 1$. According to the adopted surface temperature distribution (eq. [6]), the regions close to the equator have very low temperatures and can not be associated with any model in the archive. However, being so cool, their contribution to the observed spectrum is negligible (see §2.4). For each model the emerging radiation inten-

sity, $I_E(\tau = 0, \mu, \varphi)$, is stored, for $0.01 \text{ keV} \leq E \leq 10 \text{ keV}$, $0 \leq \mu \leq 1$ and $0 \leq \varphi \leq 2\pi$. The archive itself consists of a six-dimensional array $\mathcal{I}(B, T_s, \cos \alpha; E, \mu, \varphi)$ which associates at each set of the parameters $B, \cos \alpha, T_s$ the (discrete) values of the angle- and energy-dependent intensity. Actually, since the code makes use of adaptive computational meshes, the emerging intensities have been interpolated on common energy and angular grids before storage. The final array contains the emerging intensity for about 100 atmospheric models, evaluated at 100 energy bins and on a 20×20 angular mesh, (μ, φ) .

2.3 The Observed Spectrum

The problem of computing the pulse profile produced by hot caps onto the surface of a slowly rotating NS including gravity effects was first tackled by Pechenick, Ftaclas & Cohen (1983). Their results were then generalized to the case of emission from the entire star surface with an assigned temperature distribution by Page (1995) and Lloyd et al. (2004), in case of isotropic and non-isotropic radiation fields respectively. The approach used here follows that discussed in the two papers quoted above which we refer to for more details. For the sake of clarity, we will present a Newtonian derivation first. Relativistic ray-bending can be then accounted for quite straightforwardly.

The NS viewing geometry is described in terms of two angles χ and ξ which give the inclination of the LOS and of the dipole axis with respect to the star spin axis. Let \mathbf{z} , \mathbf{b}_{dip} and \mathbf{p} denote the unit vectors along the same three directions. Let us moreover introduce two cartesian coordinate systems, both with origin at the star center: the first, (X, Y, Z) , is fixed and such that the Z -axis coincides with the LOS while the X -axis is in the (\mathbf{z}, \mathbf{p}) plane; the second, (x, y, z) , rotates with the star. The z -axis is parallel to \mathbf{b}_{dip} while the choice of the x -axis will be made shortly. Each cartesian frame has an associated polar coordinate system, with polar axes along Z and z , respectively. The colatitude and azimuth are (Θ, Φ) in the fixed frame, and (θ, ϕ) in the rotating one (the latter are just the magnetic colatitude and azimuth introduced in § 2.1).

In the following we shall express vectors through their components: these are always the cartesian components referred to the fixed frame, unless otherwise explicitly stated. The same components are used to evaluate both scalar and vector products. Upon introducing the phase angle $\gamma = \omega t$, it follows from elementary geometrical considerations that $\mathbf{p} = (-\sin \chi, 0, \cos \chi)$ and $\mathbf{b}_{dip} = (-\sin \chi \cos \xi - \cos \chi \sin \xi \cos \gamma, -\sin \xi \sin \gamma, \cos \chi \cos \xi + \sin \chi \sin \xi \cos \gamma)$. It can be easily verified that $\mathbf{q} = (\cos \xi \sin \gamma, \cos \gamma, \sin \xi \cos \gamma)$ represents a unit vector orthogonal to \mathbf{p} and rotating with angular velocity ω . We then choose the x -axis in the direction of the (normalized) vector component of \mathbf{q} perpendicular to \mathbf{b}_{dip} ,

$$\mathbf{q}_\perp = \frac{\mathbf{q} - (\mathbf{b}_{dip} \cdot \mathbf{q}) \mathbf{b}_{dip}}{[1 - (\mathbf{b}_{dip} \cdot \mathbf{q})^2]^{1/2}}; \quad (7)$$

the y -axis is parallel to $\mathbf{b}_{dip} \times \mathbf{q}_\perp$. The local unit normal relative to a point on the star surface of coordinates (Θ, Φ) is readily expressed as $\mathbf{n} = (\sin \Theta \cos \Phi, \sin \Theta \sin \Phi, \cos \Theta)$.

By introducing the unit vector \mathbf{n}_\perp , defined in strict analogy with \mathbf{q}_\perp (see eq. [7]), the two expressions

$$\cos \theta = \mathbf{b}_{dip} \cdot \mathbf{n} \quad (8)$$

$$\cos \phi = \mathbf{n}_\perp \cdot \mathbf{q}_\perp \quad (9)$$

provide the relations between the two pairs of polar angles, the geometrical angles ξ, χ and the phase. While direct inversion of (8) poses no problems since it is $0 \leq \theta \leq \pi$, care must be taken to ensure that ϕ , as obtained from (9), covers the entire range $[0, 2\pi]$. This is achieved by replacing ϕ with $2\pi - \phi$ when $\mathbf{n} \cdot (\mathbf{b}_{dip} \times \mathbf{q}_\perp) < 0$.

We are now in the position to compute the total monochromatic flux emitted by the star and received by a distant observer. This is done by integrating the specific intensity over the visible part of the star surface at any given phase (see e.g. Lloyd et al. 2004)

$$F_E(\gamma) \propto \int_0^{2\pi} d\Phi \int_0^1 \mathcal{I}(B, T_s, \cos \alpha; E, \mu, \varphi) du^2 \quad (10)$$

where $u = \sin \Theta$. Further integration of eq. (10) over γ provides the phase-averaged spectrum. As discussed in § 2.2, the intensity depends on the properties of the surface patch and on the photon direction. The magnetic field strength B can be directly computed from the polar components of \mathbf{B} (see § 2.1 and Page & Sarmiento 1996). The magnetic tilt angle α and the surface temperature (see eq. [6]) follow from $\cos \alpha = \mathbf{n} \cdot \mathbf{B}/B = B_r/B$, being \mathbf{n} the unit radial vector. The local values of \mathbf{B} and T_s depend on (θ, ϕ) . They can be then easily expressed in terms of (Θ, Φ) for any given phase using eqs. (8)-(9). Because the star appears point-like, there is a unique ray which reaches the observer from any given surface element and this implies that also μ and φ are functions of (Θ, Φ) . It is clearly $\mu = \cos \Theta$, while φ is given by $\cos \varphi = \mathbf{m} \cdot \mathbf{v}$. The two unit vectors which enter the previous expression are, respectively, the projections of \mathbf{B} and \mathbf{z} on the plane locally tangent to the surface. They are expressed as $\mathbf{m} = (\cos \Theta \cos \Phi, \cos \Theta \sin \Phi, -\sin \Theta)$ and $\mathbf{v} = (\mathbf{B}/B - \mathbf{n} \cos \alpha)/\sin \alpha$. The cartesian components of \mathbf{B} needed to evaluate $\cos \varphi$ are derived in the Appendix.

Gravity effects (i.e. relativistic ray-bending) can be now included in a very simple way. The local value of the colatitude Θ is, in fact, related to that measured by an observer at infinity by the “ray-tracing” integral

$$\bar{\Theta} = \int_0^{1/2} u \left[\frac{1}{4} \left(1 - \frac{1}{x} \right) - \left(1 - \frac{2v}{x} \right) x^2 v^2 \right]^{-1/2} dv \quad (11)$$

where $x = R/R_S$. Since we are collecting the contributions of all surface elements seen by a distant observer, each patch is labelled by the two angles $\bar{\Theta}$ and Φ . This means that the integrand in (10) is to be evaluated precisely at the same two angles and is tantamount to replace Θ with $\bar{\Theta}$ in all previous expressions. Note, however, that the innermost integral in (10) is always computed over Θ .

Effects of radiative beaming are illustrated in fig. 2, where we compare phase average spectra and lightcurves computed by using radiative atmosphere model with those obtained under the assumption of isotropic blackbody emission. As we can see, the pulse profiles are substantially different in the two cases. Also, by accounting for radiative beaming allow to reach relatively large pulse fractions ($\sim 20\%$).

2.4 Numerical Implementation

The numerical evaluation of the phase-dependent spectrum has been carried out using an IDL script. Since our immediate goal is to check if the observed pulse profiles can be reproduced by our model, we start by computing the lightcurve in a given energy band, accounting for interstellar absorption and the detector response function. Most of the recent observations of X-ray emitting INSs have been obtained by *XMM-Newton*, so here we refer to EPIC-pn response function. Both absorption and the detector response depend upon the arrival photon energy $\bar{E} = E\sqrt{1 - 1/x}$, so the pulse profile in the $[\bar{E}_1, \bar{E}_2]$ range is given by

$$\begin{aligned} F(\gamma) &\propto \int_0^{2\pi} d\Phi \int_0^1 du^2 \int_{\bar{E}_1}^{\bar{E}_2} A(\bar{E}) \exp[-N_H \sigma(\bar{E})] \\ &\quad \times \mathcal{I}(B, T_s, \cos \alpha; E, \mu, \varphi) d\bar{E} \\ &\equiv \int_0^{2\pi} d\Phi \int_0^1 du^2 \mathcal{J} \end{aligned} \quad (12)$$

where A is the response function, N_H is the column density, and σ the interstellar absorption cross section (e.g. Morrison & McCammon 1983).

Since the energy integral \mathcal{J} does not involve geometry, it is evaluated first. We select three energy bands, corresponding to the soft (0.1–0.5 keV) and hard (0.5–1 keV) X-ray colors, and to the total range 0.1–5 keV. Results are stored as described in § 2.2 in the case of the quantity \mathcal{I} , the only difference being that energy index in the array \mathcal{J} runs now from 1 to 3 in correspondence to the three energy intervals defined above. We then introduce a $(\mu = \cos \Theta, \Phi)$ mesh by specifying 50×50 equally spaced points in the $[0, 1]$ and $[0, 2\pi]$ intervals, and interpolate the intensity array at the required values of $\mu, \mu = u$. Next, the values of $\bar{\Theta}$ relative to the u grid are computed from eq. (11). All these steps can be performed in advance and once for all, because they do not depend on the viewing geometry or the magnetic field.

Then, once the angles χ, ξ and the phase γ have been specified, the magnetic colatitude and azimuth, $\theta(\bar{\Theta}, \Phi, \gamma)$, $\phi(\bar{\Theta}, \Phi, \gamma)$ can be evaluated. We use 32 phase bins and a set of five values for each of the two angles $\chi, \xi = (0^\circ, 30^\circ, 50^\circ, 70^\circ, 90^\circ)$. The magnetic field is assigned by prescribing the strength of the quadrupolar components relative to polar dipole field, $b_i = q_i/B_p$ ($i = 1, \dots, 5$), in addition to B_p itself; in our grid, each b_i can take the values $(0, \pm 0.25, \pm 0.5)$. For each pair θ, ϕ we then compute \mathbf{B} and $\cos \varphi$; $\cos \alpha$ gives the surface temperature T_s once T_p has been chosen. The corresponding values of the intensity are obtained by linear interpolation of the array \mathcal{J} . Surface elements emitting a flux two order of magnitudes lower than that of the polar region (σT_p^4) were assumed not to give any contribution to the observed spectrum. Finally, direct numerical evaluation of the two angular integrals in (12) gives the lightcurves. Although in view of future application we computed and stored the lightcurves in the three energy bands mentioned above, results presented in § 3 and 4 are obtained using always the total (0.1–5 keV) energy band. To summarize, each model lightcurve depends on χ, ξ , and the five b_i . No attempt has been made here to vary also T_p and B_p , which have been fixed at 140 eV and 6×10^{12} G respectively. A total of 78125 models have been computed and stored. Their analysis is discussed in § 3.

3 ANALYZING LIGHTCURVES AS A POPULATION

As discussed in § 2, under our assumptions the computed lightcurve is a multidimensional function which depends in a complex way on several parameters. Therefore, an obvious question is whether or not we can identify some possible combinations of the independent parameters that are associated to particular features observed in the pulse shape. The problem to quantify the degree of variance of a sample of individuals (in our case the lightcurves) and to identify groups of “similar” individuals within a population is a common one in behavioral and social sciences. Several techniques have been extensively detailed in many books of multivariate statistics (e.g. Kendall 1957; Manly 1998) and, although they have been little used in physical sciences, a few applications to astrophysical problems have been presented over the past decades (see e.g. Whitney 1983; Mittaz, Penston & Snijders 1990; Heyer & Schloerb 1997).

We focus here on a particular tool called *principal components analysis* (PCA), which appears promising for a quantitative classification of the lightcurve features. The main goal of PCA is to reduce the number of variables that need to be considered in order to describe the data set, by introducing a new set of variables z_p (called the principal components, PCs) which can discriminate most effectively among the individuals in the sample, i.e. the lightcurves in our present case. The PCs are uncorrelated and mutually-orthogonal linear combinations of the original variables. Besides, the indices of the PCs are ordered so that z_1 displays the largest amount of variation, z_2 displays the second largest and so on, that is, $\text{var}(z_1) \geq \text{var}(z_2) \geq \dots \geq \text{var}(z_p)$ where $\text{var}(z_k)$ is the variance in the sample associated with the k -th PC. Although the physical meaning of the new variables may be in general not immediate, it often turns out that a good representation of the population is obtained by using a limited number of PCs, which allows to treat the data in terms of their true dimensionality. Beyond that, PCA represents a first step towards other kind of multivariate analyses, like the *cluster analysis*. This is a tool which allows to identify subgroups of objects so that “similar” ones belong to the same group. When applying the cluster analysis algorithm a PCA is performed first in order to reduce the number of original variables down to a smaller number of PCs. This can substantially reduce the computational time.

Since both tools are extensively described in the literature, we omit all mathematical details for which an interested reader may refer to, e.g., Kendall (1957) and Manly (1998). Let us denote with y_{ps} ($p = 1, \dots, P$; $s = 1, \dots, S$) the values of the intensity computed at each phase bin, for each model lightcurve. Let us also introduce the “centered” data x_{ps} , defined as

$$x_{ps} = (y_{ps} - \mu_p) / s_p, \quad (13)$$

where μ_p and s_p are the mean and the variance of the computed data, respectively. In order to shift to the new PCs variables z_{ps} , we computed the transformation matrix V' such that

$$z_{ps} = \sum_q v'_{pq} x_{qs}. \quad (14)$$

A sufficient condition to specify univocally V' is to impose

that the axes of the new coordinate system (i.e. the PCs) are mutually orthogonal and linearly independent.

By applying the PCA to our sample of models, we have found that each lightcurve can be reproduced using only the first 20-21 more significant PCs (instead of 32 phases) and that the first 4 PCs alone account for as much as $\sim 85\%$ of the total variance. Moreover, $\sim 72\%$ of the variance is in the first three PCs only. It is therefore meaningful to introduce a graphical representation of the model dataset in terms of the first three z_i 's. This is shown in figure 3 where black/red squares gives the position in the $z_1 z_2 z_3$ space of quadrupolar/dipolar models. To better visualize the latter, an additional set of lightcurves was computed, bringing the total number of dipolar models displayed in fig. 3 to 100.

An insight on the lightcurve property each of the PCs measures can be obtained by inspecting the coefficients v'_{pq} of the linear combination which gives the z_p 's for an assigned dataset [see eq. (14)]. Since $z_p = \sum_q v'_{pq} x_q \propto \int_0^{2\pi} v_p(\gamma) F(\gamma) d\gamma$, this is tantamount to assess the effect of the filter $v_p(\gamma)$ on the lightcurve $F(\gamma)$ knowing the values of the former at a discrete set of phases. The first four v_p are shown in Fig. 4. The first PC provides a measure of the amplitude of the pulse; it is always $z_1 > 0$, and large values of z_1 correspond to low pulsed fractions. Both z_2 and z_3 may take either sign (same for higher order PCs) and give information on the pulse shape. We note that, although the absolute phase is in principle an arbitrary quantity, the whole models population has been computed using the same value. Therefore, when studying the morphological properties of the sample of lightcurves, it is meaningful to refer to the symmetry properties with respect to the parameter γ . Large and negative values of z_2 imply that the main contributions to the lightcurve comes from phases around zero. z_3 measures the parity of the lightcurve with respect to half period. Pulses which are symmetric have $z_3 = 0$. As fig. 3 clearly shows, the PCA is very effective in discriminating purely dipolar from quadrupolar models. The former cluster in the “tip of the cloud”, at large values of z_1 , negative values of z_2 in the $z_3 = 0$ plane, as expected. In fact, dipolar pulse patterns are always symmetrical and their pulsed fraction is quite small (semi-amplitude $\lesssim 10\%$). It is worth noticing that quadrupolar magnetic configurations too can produce quite symmetrical lightcurves, e.g. the black squares in fig. 3 with $z_3 \sim 0$. However, in this case the pulsed fraction may be much larger, as indicated by the lower values of z_1 attained by quadrupolar models with $z_3 = 0$ in comparison with purely dipolar ones. This implies that a symmetrical lightcurve is not *per se* an indicator of a dipolar magnetic geometry.

As suggested by some authors (e.g. Heck 1976; Whitney 1983), PCs can then be used as new variables to describe the original data. However, in the case at hand, the problem is that although PCs effectively distinguish among pulse patterns, they have a purely geometrical meaning and can not be directly related to the physical parameters of the model (b_i, χ, ξ). We have found that the standard regression method does not allow to link the PCs with the model parameters, which is likely to be a signature of a strong non-linearity (see § 5). Instead, the PCA can be regarded as a method to provide a link between the numerous lightcurves, in the sense that models “close” to each other in the PCs

space will have similar characteristics. Unfortunately, despite different definitions of metrics have been attempted, so far we found it difficult to translate the concept of “proximity” in the PCs space in a corresponding “proximity” in the 7-dimensional space of the physical parameters ξ, χ and b_i ($i = 1, \dots, 5$). By performing a cluster analysis we found that two separate subgroups are clearly evident in the PCs space, one of which encompasses the region occupied by purely dipolar models (see fig. 5, top panel). However, again it is not immediate to find a corresponding subdivision in the physical space. Due to these difficulties, we postpone a more detailed statistical analysis to a follow-up paper, and, as discussed in the next section, we concentrate on the direct application of our models to the observed lightcurves of some isolated neutron stars.

4 AN APPLICATION TO XDINSS

In the light of the discussion at the end of the previous section, the PCA may be used to get insights on the ability of the present model to reproduce observed lightcurves. A simple check consists in deriving the PC representation of the pulse profiles of a number of sources and verify if the corresponding points in the $z_1 z_2 z_3$ space fall inside the volume covered by the models. We stress once again that, although the model lightcurves depend upon all the PCs, z_1, z_2 , and z_3 alone provide a quite accurate description of the dataset since they account for a large fraction of the variance. In this sense the plots in fig. 3 give a faithful representation of the lightcurves, with no substantial loss of information: profiles close to each other in this 3-D space exhibit a similar shape. To this end, we took the published data for the first four pulsating XDINSSs listed in table 1 and rebinned the lightcurves to the same 32 phase intervals used for the models. Since the PCA of the model dataset already provided the matrix of coefficients v'_{pq} (see eq. [14]), the PCs of any given observed lightcurve are $z_p^{obs} = \sum_q v'_{pq} x_q^{obs}$, where x_q^{obs} is the (standardized) X-ray intensity at phase γ_q . As it can be seen from fig. 3, the observed pulse profiles never fall in the much smaller region occupied by purely dipolar models. However, they all lie close to the quadrupolar models, indicating that a quadrupolar configuration able to reproduce the observed features may exist. A possible exception to this is the first observation of RX J0720.4-3125 (*XMM-Newton* rev. 078), for which the pulse profile appears quite symmetric and the pulsed fraction is relatively small (see table 1). While a purely dipolar configuration may be able to reproduce the lightcurve for rev. 078, a visual inspection of fig. 3 shows that this is not the case for the second observation of the same source (*XMM-Newton* rev. 711). Despite the pulse shape is still quite symmetrical, the pulsed fraction is definitely too large to be explained, within the current model, with a simple dipole field. The same considerations apply to the lightcurve of RX J0420.0-5022.

Just as a counter-example, we added in fig. 3 the PC representation of the X-ray lightcurve of the Anomalous X-ray pulsar 1E 1048.1-5937 observed in two different epochs, 2000 December and 2003 June (see Mereghetti et al. 2004). The new data points fall well outside the region of the population of quadrupolar models and can be seen only in the last panel of fig. 3. In the case of this source, the pulsed fraction

is so high (89% and 53% in June and December respectively) that no quadrupolar configuration could account for it. In terms of PCs, both points have a relatively low value of z_1 ($z_1 = 9.9$ and $z_1 = 6.9$). In this case no fit can be found, not surprisingly, since we do expect a large contribution from a non-thermal power law component to the X-ray emission of Anomalous X-ray pulsars.

To better understand to which extent quadrupolar surface distributions may indeed produce lightcurves close to the observed ones, we select the model in the data set which is “closer” to each of the observed lightcurves. This is done looking first for the minimum Euclidean distance between the observed and the model pulse profiles in the PCs space. Note that in this case all the relevant PCs were used, that is to say the distance is defined by $D^2 = \sum_{p=1}^{20} (z_p - z_p^{obs})^2$. The computed model which minimizes D is then used as the starting point for a fit to the observed lightcurve which yields the best estimate of the model parameters. The fitting is performed by computing “on the fly” the lightcurve for the current values of the parameters and using the standard (i.e. not the PC) representation of both model and data. The quadrupolar components and viewing angles are treated as free parameters while the polar values T_p and B_{dip} are fixed and must fall in the domain spanned by our atmosphere model archive.¹ The (arbitrary) initial phase of the model is an additional parameter of the fit.

The results of the fits are shown in figures 5, 6 and 7 for $B_{dip} = 6 \times 10^{12}$ G, $\log T_p$ (K) = 6.1 – 6.2. It is apparent that the broad characteristics of all the XDINSs lightcurves observed so far may be successfully reproduced for a suitable combination of quadrupolar magnetic field components and viewing angles. However, although in all cases a fit exists, we find that in general it is not necessary unique. This means that the model has no “predictive” power in providing the exact values of the magnetic field components and viewing angles. For this reason we do not attempt a more complete fit, i.e. leaving also T_p and B_{dip} free to vary, nor we derive parameter uncertainties or confidence levels. Our goal at this stage has been to show that there exist at least one (and more probably more) combination(s) of the parameters that can explain the observed pulse shapes, while this is not possible assuming a pure dipole configuration.

The case of RX J0720.4-3125 deserves, however, some further discussion. This source, which was believed to be stationary and as such included among *XMM-Newton* EPIC and RGS calibration sources, was recently found to exhibit rather sensible variations both in its spectral and timing properties (De Vries et al. 2004; Vink et al. 2004). In particular, the pulse shape changed over the ~ 2 yrs time between *XMM* revolutions 78 and 711. De Vries et al. (2004) proposed that the evolution of RX J0720.4-3125 may be produced by a (freely) precessing neutron star. This scenario can be tested by our analysis, since in a precessing NS only the two angles ξ and χ are expected to vary while the magnetic field remains fixed. This means that having found one combination of parameters which fits the lightcurve of rev.

78, a satisfactory fit for rev. 711 should be obtained for the same b_i ’s and different values of the angles. Despite several attempts, in which the proper values of T_p as derived from the spectral analysis of the two observations were used, we were unable to obtain a good fit varying the angles only (see figure 8). We performed also a simultaneous fit to both lightcurves starting from a general trial solution and asking that the b_i ’s are the same (but not necessarily coincident with those that best fit data from rev. 78), while the two angles (and the initial phases) are kept distinct (see figure 9). Both approaches clearly indicate that a change in both sets of quantities (magnetic field and angles) is required (as in Fig. 7). From a physical point of view it is not clear how magnetic field variations on such a short timescale may be produced, therefore at present no definite conclusion can be drawn. For instance, one possibility that makes conceivable a change of the magnetic field structure and strength on a timescale of years is that the surface field is small scaled (Geppert, Rheinhardt & Gil 2003). In this case, even small changes in the inclination between line of sight and local magnetic field axis may cause significant differences in the “observed” field strength.

5 DISCUSSION

X-ray dim isolated neutron stars (XDINSs) may indeed represent the Rosetta stone for understanding many physical properties of neutron stars at large, including their equation of state. Despite their potential importance, only recently detailed observations of these sources have become progressively available with the advent of *Chandra* and *XMM-Newton* satellites. These new data, while confirming the thermal, blackbody-like emission from the cooling star surface, have revealed a number of spectral and timing features which opened a new window on the study of these objects. Some issues are of particular importance in this respect: i) the discovery of broad absorption features at few hundreds eVs, ii) the quite large pulsed fractions, iii) the departure of the pulse shape from a sine wave, and iv) the long-term evolution of both the spectral and timing properties seen in RX J0720.4-3125 and, to some extent, in RX J0420.0-5022. Pulse-phase spectroscopy confirms that spectral and timing properties are interwoven in a way which appears more complex than that expected from a simple misaligned rotating dipole, as the anti-correlation of the absorption line strength and of the hardness ratio with the intensity along the pulse testify.

Motivated by this, we have undertaken a project aimed at studying systematically the coupled effects of: i) radiative transfer in a magnetized atmospheric layer, ii) thermal surface gradients, and iii) different topologies of the surface magnetic field in shaping the spectrum and pulse shape. The ultimate goal of our investigation is to obtain a simultaneous fit of both pulse profile and (phase-averaged and -resolved) spectral distribution. As detailed comparisons of synthetic spectra with observations have shown, no completely satisfactory treatment of spectral modelling for these sources is available as yet. For this reason, here we presented the general method and concentrated on the study of the lightcurves, computed assuming a pure H, magnetized at-

¹ In general this will not contains the exact values inferred from spectral observations of XDINSs. However, we have checked that a fit (albeit with different values of the quadrupolar field) is possible for different combinations of B_{dip} and T_p in the range of interest.

mosphere. The pulse shapes, in fact, should be less sensitive on the details of the chosen atmospheric model.

We caveat the reader that our results have been computed under a number of simplifying assumptions. For instance, there are still considerable uncertainties in current modelling of the NS surface thermal emission: we just mention here that most of the observed NS spectra cannot be reproduced by the theoretical models currently available (see Haberl 2003, Haberl 2004 for reviews and references therein). Second, the surface temperature has been derived using eq. (5) which is based on the assumption that the temperature profile is only dictated by the heat transferred from the star interior. While this is expected to be the main mechanism, other effects may significantly contribute. For instance, heating of the star surface may occur because of magnetic field decay, and the polar caps may be re-heated by back-flowing particles or by internal friction. Third, we have computed the emissivity by assuming that each atmospheric, plane parallel, patch emits a total flux σT_s^4 . In other words, while the spectral distribution is computed using a proper radiative transfer calculation, we introduced the further assumption that each slab emits the same total flux as a blackbody radiator. A more consistent approach would be to compute the spectrum emitted by each patch by taking the value of T_s and the efficiency of the crust as a radiator (Turolla, Zane & Drake 2004) as the boundary condition at the basis of the atmosphere. Our working assumption avoids the burden of creating a complete grid of models in this parameter, with the disadvantage that the spectral properties of each patch may be slightly approximated.

As far as the application to XDINSs is concerned, the greatest uncertainties arise because in this paper we are not fitting simultaneously the observed spectra and pulse shape. The quadrupolar components and viewing angles are treated as free parameters while the polar values T_p and B_{dip} are fixed and, of course, they must fall in the domain spanned by our atmosphere model archive. As stated earlier, albeit we have checked that a fit is possible for different combinations of B_{dip} and T_p in the allowed range, in general the archive will not contain the exact values of T inferred from spectral observations of the coldest XDINSs. As long as we make the same assumption that the local spectrum emitted by each patch of the star surface is computed using fully ionized, magnetized hydrogen atmosphere models, we do still expect to reach a good fit by using a temperature of a few tens of eV smaller than those used, albeit with different values of the quadrupolar components. However, partial ionization effects are not included in our work, and bound atoms and molecules can affect the results, changing the radiation properties at relatively low T and high B (Potekhin & Chabrier 2003; Potekhin et al. 2004).

Even more crucial is the issue of fitting with a realistic value of the magnetic field. The recent detection of absorption features at $\approx 300\text{--}700$ eV in the spectrum of XDINSs and their interpretation in terms of proton cyclotron resonances or bound-bound transitions in H or H-like He, may indicate that these sources possess strong magnetic fields, up to $B \sim 9 \times 10^{13}$ G (Van Kerkwijk et al. 2004; Haberl et al. 2004; Zane et al. 2005). A (slightly) more direct measurement, based on the spin-down measure, has been obtained so far only in one source (i.e. RX J0720.4-3125, e.g. Cropper et al. 2004, Kaplan & van Kerkwijk 2004). In

this case the measurement points at a more moderate field, $B \sim (2 - 3) \times 10^{13}$ G, which is only a few times larger than that used here. However, the possibility that (some) of these objects are ultra-magnetized NSs is real. Would this be confirmed, our model archive should be extended to include higher field values. This, however, poses a serious difficulty, since the numerical convergence of model atmospheres is particularly problematic at such large values of B for $T \lesssim 10^6$ K. Moreover, as mentioned in §2.1, if such high field strengths are associated to crustal (and not to star-centered) fields, the surface temperature gradient is expected to be substantially different from that used in the present investigation (Geppert, Küker & Page 2004).

The application presented here makes only use of the properties of the pulse profile in the total energy band, and does not exploit color and spectral information available for these sources. This worsens the problem of finding a unique representation, problem which is to some extent intrinsic, due to the multidimensional dependence of the fitting function on the various physical parameters. Aim of our future work is to reduce the degeneracy by refining the best fit solutions by using information from the light curves observed in different color bands and/or from the spectral line variations with spin pulse. Also, a more detailed statistical analysis on the models population based on algorithms more sophisticated than the PCA's (Gifi 1990; Saegusa 2005) may shed light on the possible correlation between the physical parameters in presence of strong non-linearity and possibly on the meaning of the two subclasses identified through a cluster analysis.

6 ACKNOWLEDGEMENTS

We acknowledge D.A. Lloyd and R. Perna for allowing us to use their radiative transfer code (which accounts for a non vanishing inclination between the local magnetic field and the local normal to the NS surface), for their assistance in the set up and for several discussions during the early stages of this investigation. Work partially supported by the Italian Ministry for Education, University and Research (MIUR) under grant PRIN 2004-023189. SZ thanks PPARC for its support through a PPARC Advanced Fellowship.

REFERENCES

- Burwitz V., et al., 2003, *A&A*, 399, 1109
- Cadeau C., Leahy D.A., Morsink S.M., 2005, *ApJ*, 618, 451
- Cropper M., et al., 2001, *A&A*, 365, L302
- Cropper M., Haberl F., Zane S., Zavlin V.E., 2004, *MNRAS*, 351, 1099
- De Vries C.P., et al., 2004, *A&A*, 415, L31
- Geppert U., Rheinhardt M., Gil, J., 2003, *A&A*, 412, L33
- Geppert U., Küker M., Page D., 2004, *A&A*, 426, 267
- Gifi A., 1990, *Nonlinear multivariate analysis*. Wiley, New York
- Greenstein G., Hartke G.J., 1983, *ApJ*, 271, 283
- Haberl F., 2003, In proceedings of the Cospar Symposium on High Energy Studies of Supernova Remnants and Neutron Stars, MPE, Garching (astro-ph/0302540)
- Haberl F., et al., 2003, *A&A*, 403, L19

- Haberl F., 2004, *Adv. Sp. Research*, 33, 638
Haberl F., et al., 2004, *A&A*, 424, 635
Heck A., 1976, *A&A*, 47, 129
Heyer M.H., Schloerb, F.P., 1997, *ApJ*, 475, 173
Heyl J.S., Hernquist, L., 1998, *MNRAS*, 300, 599
Ho W.C.G. & Lai D., 2003, *MNRAS*, 327, 1081
Ho W.C.G., Lai, D., 2003, *MNRAS*, 338, 233
Ho W.C.G, Lai D., Potekhin, A.Y., Chabrier G., 2003, *ApJ*, 599, 1293
Kaplan, D., van Kerkwijk, M.H., 2004, *ApJL*, in press (astro-ph/0506419)
Kendall M.G., 1957, *A Course in Multivariate Analysis*. Griffin & Co., London
Lloyd D.A., 2004, *MNRAS*, submitted, (astro-ph/0303561)
Lloyd D.A., Perna R., Slane P., Nicastro F., Hernquist L., 2004, *ApJ*, submitted, (astro-ph/0306235)
Manly B.F.J., 1998, *Multivariate Statistical Methods, A Primer*. Chapman & Hall, New York
Mereghetti, S., Tiengo, A., Stella, L., Israel, G.L., Rea, N., Zane, S., Oosterbroek, T., *ApJ*, 608, 427
Mittaz J.P.D., Penston M.V., Snijders, M.A.J., 1990, *MNRAS*, 242, 370
Morrison R., McCammon D., 1983, *ApJ*, 270, 119
Page D., 1995, *ApJ*, 442, 273
Page D., Sarmiento A., 1996, *ApJ*, 473, 1067
Pavlov G.G, Shibano Yu.A., Ventura J., Zavlin V.E., 1994, *A&A*, 289, 837
Pechenick K.R., Ftaclas C. & Cohen J.M., 1983. *ApJ*, 274, 846
Potekhin A.Y., Chabrier G., 2003, *ApJ*, 585, 955
Potekhin A.Y., Lai D., Chabrier G., Ho W.C.G., 2004, *ApJ*, 612, 1034
Schwope A.D., Hambaryan V., Haberl F., Motch C., 2005, *A&A*, in press (astro-ph/050538)
Saegusa R., 2005, unpublished PhD thesis (available at <http://www.sri-report.com/strage/dissertation/main.html>)
Shibanov Yu.A., Zavlin V.E., Pavlov G.G., Ventura, J., 1992, *A&A*, 266, 313
Treves A., Turolla R., Zane S., Colpi, M., 2000, *PASP*, 112, 297
Turolla R., Zane S., Drake J.J., 2004, *ApJ*, 603, 265
Urpín V., Gil J., 2004, *A&A*, 415, 305
Van Kerkwijk M.H., et al., 2004, *ApJ*, 608, 432
Vink J., et al., 2004, *ApJ*, 609, L75
Whitney C.A., 1983, *A&A Suppl.*, 51, 443.
Zane S., Turolla R., Stella L., Treves A., 2001, *ApJ*, 560, 384
Zane S., et al., 2005, *ApJ*, 627, 397

Isolated Neutron Stars Parameters.				
Source	P (s)	Semi-Ampl.	XMM-Newton rev.	Refs.
RX J0420.0-5022	3.45	13%	570	1
RX J0806.4-4123	11.37	6%	618	1
RBS 1223	10.31	18%	561	2
RX J0720.4-3125	8.39	11%	78	3
RX J0720.4-3125	8.39	16%	711	3
RBS 1774	9.44	4%	820	4

Table 1. The light curves used in this paper are taken from references listed in the fourth column, which correspond to: [1] Haberl et al. (2004); [2] Haberl et al. (2003); [3] De Vries et al. (2004); [4] Zane et al. (2005).

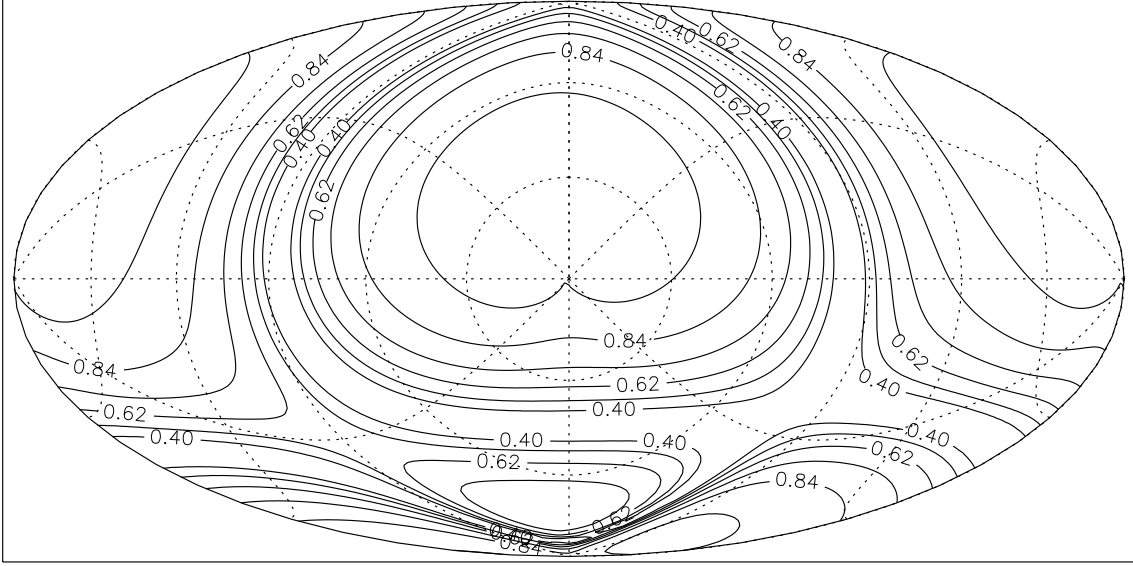


Figure 1. Hammer projection illustrating the thermal surface distribution of a NS; the quadrupolar field components (in units of the polar dipolar field) are $b_0 = 0.0248$, $b_1 = 0.684$, $b_2 = 0.0501$, $b_3 = 0.0480$, $b_4 = -0.0624$. The contours are labelled by the values of T_s/T_p .

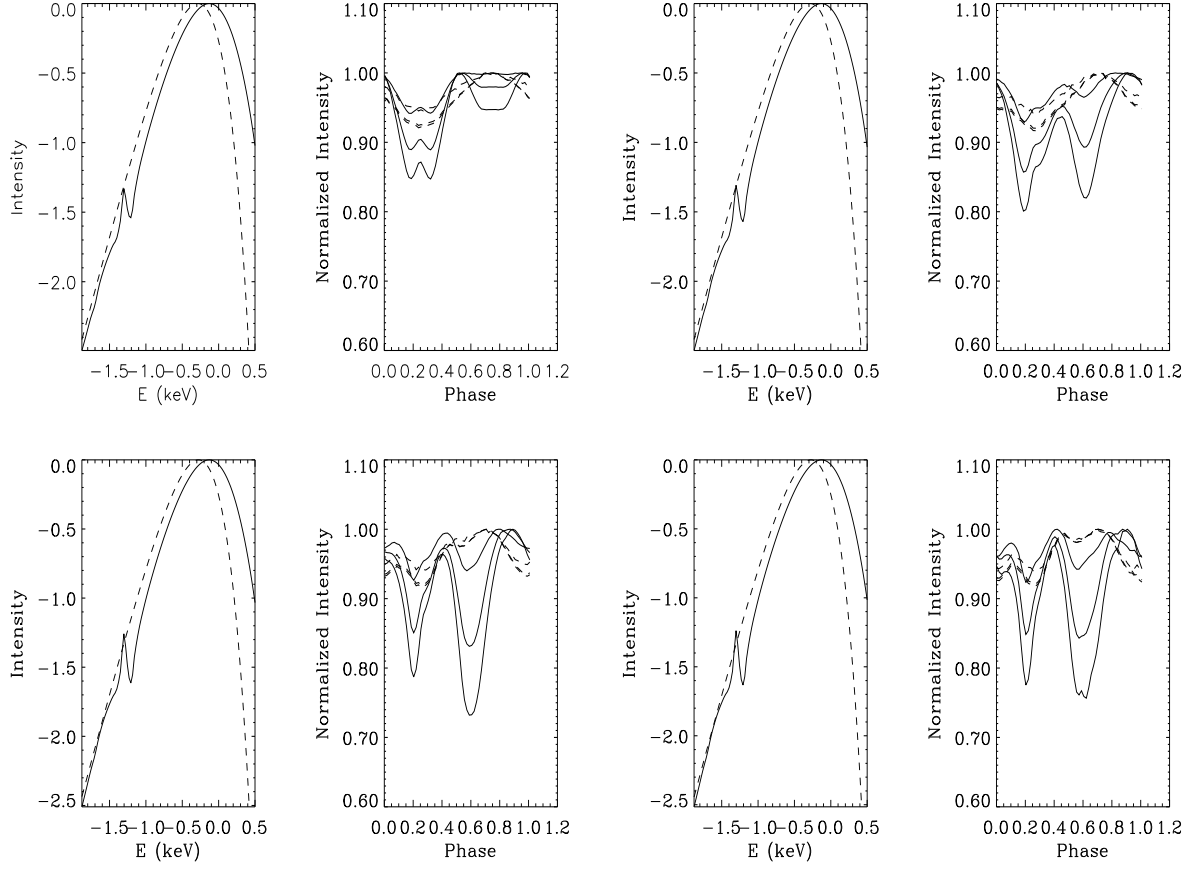


Figure 2. Effects of Radiative beaming. In each pair of figures we show phase average spectrum (left) and light curves in the 0.1-2 keV, 0.1-0.5 keV and 0.5-2 keV bands (right, arbitrary normalization). In all panels solid lines refer to atmospheric models, while dashed lines to blackbody emission. The four pairs of figures correspond to different values of ξ : from top left to bottom right it is $\xi = 0^\circ, 30^\circ, 60^\circ, 90^\circ$, respectively. The remaining parameters are fixed at: $B_{dip} = 6 \times 10^{12}$ G, $T_{pol} = 2.5$ MK, $b_0 = 0.5$, $b_1 = b_3 = b_4 = 0$, $b_2 = 0.9$, $\chi = 90^\circ$.

This figure is provided separately as the f3.png file

Figure 3. The computed population of lightcurves plotted against the first 3 principal components; units on the axes are arbitrary. Yellow symbols mark the position of the EPIC-PN light curves of XDINSs (both observations relative to rev. 78 and rev. 711 are shown for RX J0720.4-3125), red symbols mark the lightcurves computed assuming a pure dipolar field. The PCs representation (limited to the first three PCs, which alone account for the 72% of the total variance) of the observed lightcurves falls within the domain spanned by the quadrupolar model representations; this is why at least one fitting solution can be found. For comparison, the position of the EPIC-PN lightcurves of the Anomalous X-ray pulsar 1E 1048.1-5937 is also shown. These two points fall outside the model distribution and they can be seen only in the last panel (violet diamonds; see text for details).

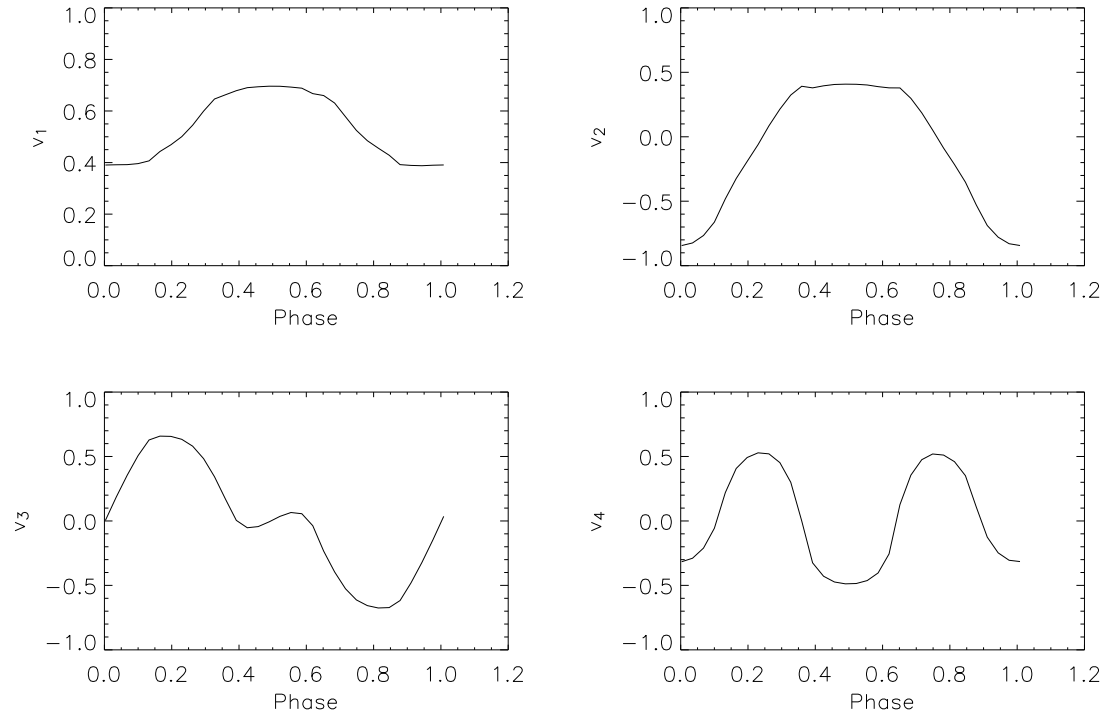


Figure 4. The first four coefficients v_p ($p = 1 \dots 4$) with respect to the phase γ . See text for all details.

The top panel of fig.5 is provided separately
as the f5a.png file

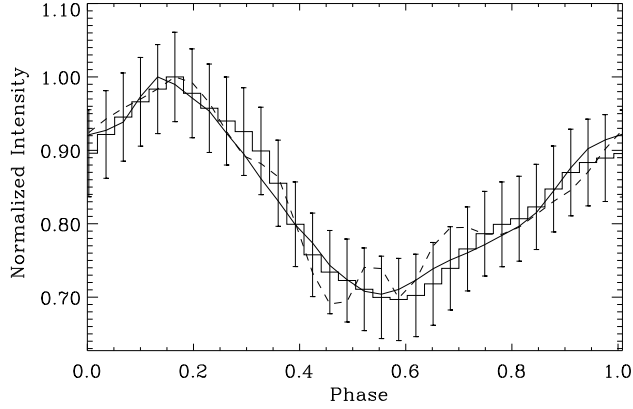


Figure 5. Top: Results of a cluster analysis performed on the models population. As in fig. 3, axis are the first three PCs: the different scale is due to the fact that here the PCs have been computed on the centered data. Two separate subgroups, plotted in red and blue respectively, are evident in the PCs space. Bottom: Fit of the EPIC-PN (0.12-0.7 keV) lightcurve of RX J0420.0-5022 detected during rev. 570 (Haberl et al. 2004). Data point refer to the smoothed observed lightcurve; dashed line: trial solution as inferred from the closest model in the PCs space; solid line: best fit solution. The best fit parameters are: $b_0 = -0.48$, $b_1 = 0.02$, $b_2 = -0.25$, $b_3 = 0.35$, $b_4 = -0.20$, $\xi = 39.9^\circ$, $\chi = 91.2^\circ$.

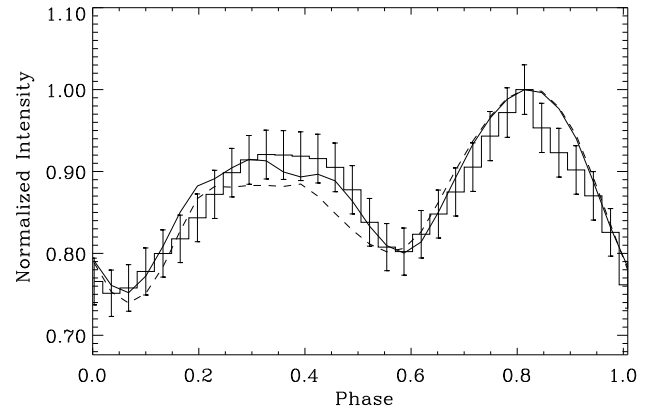
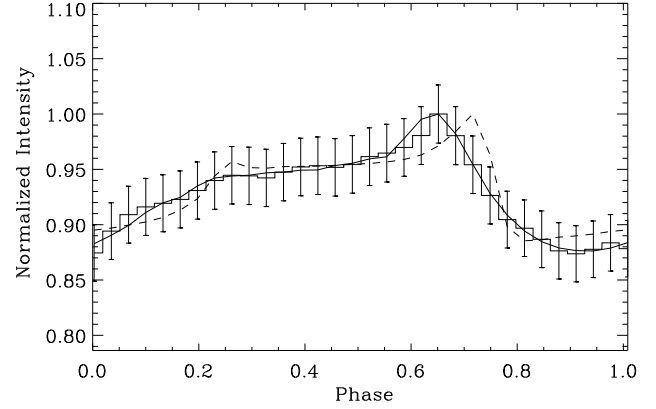


Figure 6. Same as in fig. 5 for two further XDINSs. Top: the EPIC-PN (0.12-1.2 keV) lightcurve of RX J0806.4-4123 detected during rev. 618 (Haberl et al. 2004). The best fit parameters are: $b_0 = 0.39$, $b_1 = -0.37$, $b_2 = 0.12$, $b_3 = -0.13$, $b_4 = 0.49$, $\xi = 0.0^\circ$, $\chi = 59.2^\circ$. Bottom: the EPIC-PN (0.12-0.5 keV) lightcurve of RBS 1223 detected during rev. 561 (Haberl et al. 2003). Best fit parameters are: $b_0 = 0.21$, $b_1 = 0.02$, $b_2 = 0.59$, $b_3 = 0.53$, $b_4 = 0.50$, $\xi = 0.0^\circ$, $\chi = 95.1^\circ$.

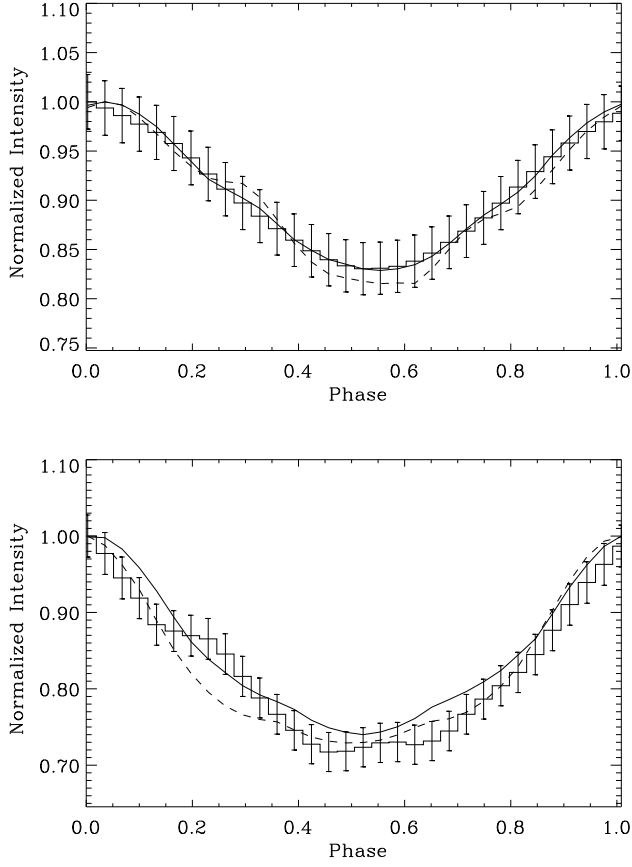


Figure 7. Same as in fig. 5 for two different EPIC-PN (0.12-1.2 keV) lightcurves detected from RXJ0720.4-3125 (both from De Vries et al. 2004). Top (rev. 78): $b_0 = 0.36$, $b_1 = 0.43$, $b_2 = -0.16$, $b_3 = -0.16$, $b_4 = -0.39$, $\xi = 0.0^\circ$, $\chi = 68.1^\circ$. Bottom (rev. 711): $b_0 = 0.45$, $b_1 = 0.49$, $b_2 = -0.06$, $b_3 = -0.08$, $b_4 = -0.26$, $\xi = 0.0^\circ$, $\chi = 87.6^\circ$. The second fit is obtained by leaving all parameters free with respect to the solution shown in the top panel.

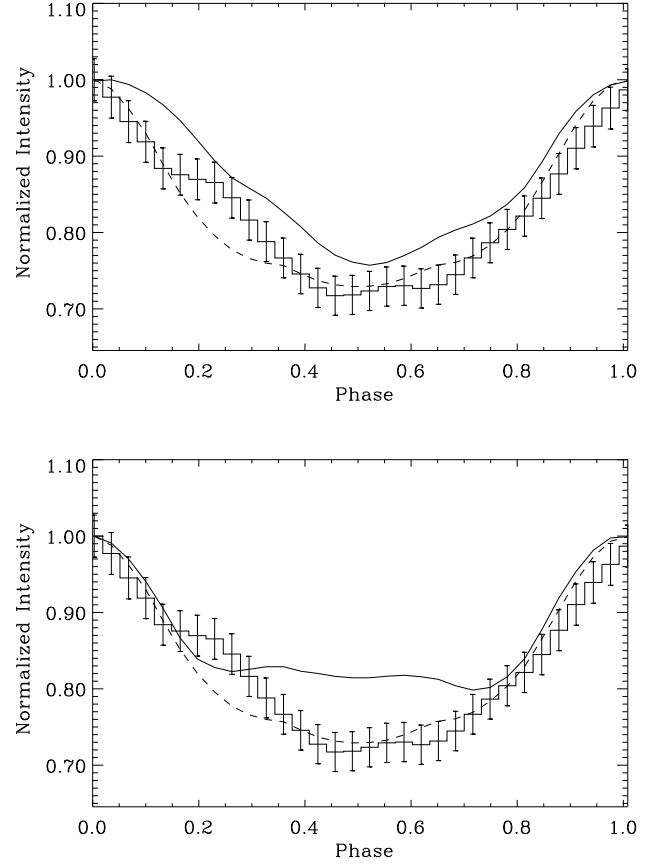


Figure 8. An attempt to fit the EPIC-PN (0.12-1.2 keV) lightcurves detected from RXJ0720.4-3125 during rev. 711 by using a fitting function with either the two viewing angles (top) or the values of b_i 's ($i = 0..4$, bottom) kept fixed and equal to the values derived in the case of rev. 78. The dashed line is the same as in Fig. 7, lower panel. In this particular example, we also allowed a fractional change of $\sim 20\%$ in the temperature between the two revolutions. Both attempts give an unsatisfactory result.

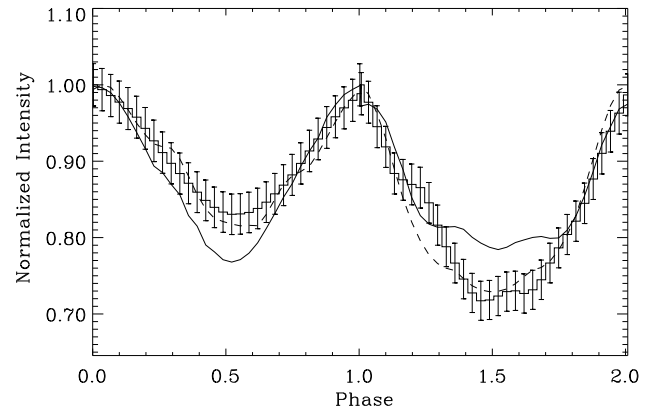


Figure 9. A simultaneous fit to both lightcurves detected from RXJ0720.4-3125 during rev. 78 (shown in the phase interval 0-1) and rev. 711 (phase 1-2). Only changes in the viewing angles have been allowed between the two epochs. The result is unsatisfactory.

APPENDIX A:

Let us write the magnetic field at any given point on the star surface in terms of its cartesian components relative to the rotating frame (x, y, z)

$$\mathbf{B} = B_x \mathbf{q}_\perp + B_y (\mathbf{b}_{dip} \times \mathbf{q}_\perp) + B_z \mathbf{b}_{dip}. \quad (\text{A1})$$

The three unit vectors which identify the cartesian axes in the rotating frame have polar components r, θ, ϕ (relative to the same frame)

$$\begin{aligned} \mathbf{q}_\perp &= (\sin \theta \cos \phi, \cos \theta \cos \phi, -\sin \theta \sin \phi) \\ \mathbf{b}_{dip} \times \mathbf{q}_\perp &= (\sin \theta \sin \theta, \cos \theta \sin \phi, \sin \theta \cos \phi) \\ \mathbf{b}_{dip} &= (\cos \theta, -\sin \theta, 0). \end{aligned} \quad (\text{A2})$$

Taking the scalar product of $\mathbf{B} = (B_r, B_\theta, B_\phi)$ with each of the three unit vectors above, we have

$$\begin{aligned} B_x &= B_r \sin \theta \cos \theta + B_\theta \cos \theta \cos \phi - B_\phi \sin \theta \sin \phi \\ B_y &= B_r \sin \theta \sin \theta + B_\theta \cos \theta \sin \phi + B_\phi \sin \theta \cos \phi \quad (\text{A3}) \\ B_z &= B_r \cos \theta - B_\theta \sin \theta. \end{aligned}$$

The cartesian components of \mathbf{B} in the fixed frame are then given by

$$\begin{aligned} B_X &= B_x (\mathbf{q}_\perp)_X + B_y (\mathbf{b}_{dip} \times \mathbf{q}_\perp)_X + B_z (\mathbf{b}_{dip})_X \\ B_Y &= B_x (\mathbf{q}_\perp)_Y + B_y (\mathbf{b}_{dip} \times \mathbf{q}_\perp)_Y + B_z (\mathbf{b}_{dip})_Y \\ B_Z &= B_x (\mathbf{q}_\perp)_Z + B_y (\mathbf{b}_{dip} \times \mathbf{q}_\perp)_Z + B_z (\mathbf{b}_{dip})_Z. \end{aligned} \quad (\text{A4})$$

This figure "f3.png" is available in "png" format from:

<http://arxiv.org/ps/astro-ph/0510693v1>

This figure "f5a.png" is available in "png" format from:

<http://arxiv.org/ps/astro-ph/0510693v1>